Received: 18 February 2020 | Revised: 3 May 2020 | Accepted: 19 May 2020

DOI: 10.1002/suco.202000105

fib CEB-FIP WILEY

TECHNICAL PAPER

Influence of production parameters on the fiber geometry and the mechanical behavior of ultra high performance fiber-reinforced concrete

Kasem Maryamh[1] | **Konstantin Hauch**[2] | **Claudia Redenbach**[2] | **Jürgen Schnell**[1]

[1]Faculty of Civil Engineering, Technische Universität Kaiserslautern, Institute of Concrete Structures and Structural Design, Kaiserslautern, Germany

[2]Department of Mathematics, Technische Universität Kaiserslautern, Kaiserslautern, Germany

Correspondence
Kasem Maryamh, Faculty of Civil Engineering, Technische Universität Kaiserslautern, Institute of Concrete Structures and Structural Design, Paul-Ehrlich-Straße 14, D-67663 Kaiserslautern, Germany.
Email: kasem.maryamh@bauing.uni-kl.de

Funding information
Deutsche Forschungsgemeinschaft, Grant/Award Number: RTG 1932

Abstract

In this paper, the relationship between production parameters of ultra high performance fiber-reinforced concrete (UHPFRC) and the spatial distribution and orientation of the steel fibers is investigated. UHPFRC specimens with varying fiber diameter, fiber volume fraction, and rheology of the mixture are produced. Additionally, casting is performed from the side or the middle of the formwork. Imaging by micro computed tomography allows for a statistical analysis of the spatial arrangement of the fibers in the test specimens. The flexural behavior and the load capacity of the specimens are analyzed by four point bending tests. The results of the bending tests are well explained by characteristics of the fiber systems determined from the image data.

KEYWORDS

consistency, fiber geometry, flexural strength, micro computed tomography, quantitative image analysis

1 | INTRODUCTION

Ultra-high performance concretes (UHPCs) are new types of cementitious materials combining a compressive strength of more than 150 N/mm^2 with a high bulk density and a low air void content. The latter is explained by the high packing density and a water-binder value below 0.25. Maximum grain sizes in UHPC are mostly limited to 0.6–1 mm. However, experiments with maximal grain sizes up to 8 or 16 mm have also been performed.[1] In practice, the optimization of the packing density of the cementitious paste is crucial. The optimum concrete can be produced by the combination of the optimum paste with the optimum aggregates for different maximum grain sizes.[1,2]

Many researchers[1,3–6] have shown that the addition of steel fibers to the UHPC is indispensable to increase the ductility of the material. As standard, micro wire fibers are used in fiber reinforced UHPC (UHPFRC). The mechanical behavior of the UHPC under different loading cases critically depends on the spatial arrangement of the fibers. For an optimal performance, fibers should be aligned to the tension direction.[7]

For analyzing the influence of production parameters on the resulting fiber geometry, the fiber system has to be observed and characterized. In particular, the orientation

Discussion on this paper must be submitted within two months of the print publication. The discussion will then be published in print, along with the authors' closure, if any, approximately nine months after the print publication.

distribution of the fibers should be investigated. This is possible by using photo-optical, magnetic or micro computed tomography (μCT) methods. The most accurate characterization is obtained by quantitative analysis of μCT images which allow for a reconstruction of the whole fiber system in 3D.[8,9]

UHPCs are typically produced with a very flowable consistency. The continuous development of PCE-plasticizers allows for a control of the viscosity of the mixture such that concrete with a wide range of consistencies can be produced. Moreover, rheological adjustments of the binder paste have been applied to optimize the deaeration behavior of the mixture.[10] Hence, besides optimization of the packing density, the rheological properties of the UHPFRC yield an important parameter that can be varied in concrete production. The fiber geometry is significantly influenced by the rheological properties of the mixture. Fiber orientation in a preferred direction can usually only be achieved by a very fluid consistency, which, however, enhances the tendency of the fibers to sediment. A homogeneous spatial distribution over the component height may then no longer be ensured.[6] Wang et al.[11] studied the dependence of the fiber distribution on the concrete rheology which was modified by varying the water-binder ratio and the amount of superplasticizer. Fiber systems were analyzed by using 2D images of sections through the samples. It turned out that moderate rheology parameters yield the most homogeneous fiber systems. Stähli et al.[12] present a study analyzing the fiber systems in three different concrete mixtures. Concrete samples were imaged by computed tomography. The analysis, however, was restricted to sectional images.

Various further production parameters may also influence the fiber geometry. Vandewalle et al.[13] investigated the influence of the flow distance, the type of concrete, and the fiber length. The latter was shown to have a negligible influence on the fiber alignment. In the work by Ferrara et al.,[14] 30 mm thin concrete slabs were produced using different casting directions. The results indicate that the casting process is an additional factor influencing the resulting fiber geometry and, hence, the bending performance. As in Wang et al.[11] the fiber orientations were determined in 2D cross sections of the specimens.

In this work, we aim at an investigation of relations between production parameters, the fiber geometry, and the mechanical properties of the concrete. For this purpose, a large number of prismatic UHPFRC specimens were produced by varying the diameter and volume fraction of the steel fibers, the consistency of the mixture and the casting point. Subsequently, the specimens were imaged by micro-computed tomography to characterize the resulting fiber geometries. Finally, correlations between production parameters, the fiber geometry, and the load-bearing behavior observed in four-point bending tests were derived.

2 | EXPERIMENTAL PROGRAM

2.1 | Production of UHPFRC

UHPC mixtures based on the M3Q-mixture with a maximum grain size of 1 mm were used. The mixture mass fractions for mixture M00 are provided in Table 1. To vary the rheology of the concrete, also specimens with an increased amount of PCE-plasticizer were considered. In the mixtures M02 and M04, the PCE content was increased by 10%, resulting in 30.25 g/L, and 20%, resulting in 33 g/L, respectively, compared to M00.

An Eirich-Intensiv mixer of 5 L volume capacity was used. Dry components were first mixed for approximately 2 min with a rotation velocity of 250 r/min. After that, both water and PCE were added after increasing the velocity to 500 r/min. Mixing was continued for 2 min, followed by a break of 2 min to scrape off dry particles. Finally, the mixture was mixed at a low velocity of 100 r/min for 7 min for deaeration. During the deaeration phase, straight brass coated wire steel fibers were added to the mixture through the shaft on top of the mixer. The fiber diameters were either $d_f = 0.2$ mm (denoted by 02)

TABLE 1 Constituents of the UHPC-mixture M00

Material	Amount (g/l)
Cement CEM I 52.5 R SR3- NA (Sulfo 5R)	825
Quarz Sand 0.125/0.5 Haltern	975
Quarz Flour-MILLISIL-W12	200
Silica fume: Sika Silicoll P uncompacted	175
Water	179
PCE-plasticizer—Sika Viscocrete 2810	27.5

Abbreviation: UHPC, ultra-high performance concrete.

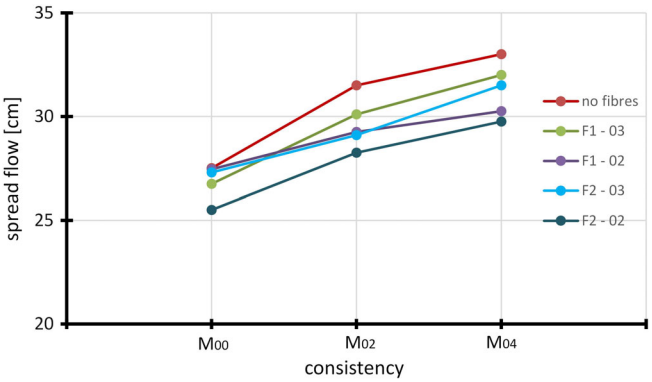

FIGURE 1 Spread flow of the UHPFRC mixture of each configuration. UHPFRC, ultra high performance fiber-reinforced concrete

or $d_f = 0.3$ mm (denoted by 03), the fiber length was 12.5 mm ($l_f/d_f = 12.5/0.2$ mm and 12.5/0.3 mm), and the fiber volume fraction was chosen as either 1% (denoted by F1) or 2% (denoted by F2). The fiber material has an ultimate tensile strength of 2.800 N/mm^2 and an elasticity modulus of 200 GPa.

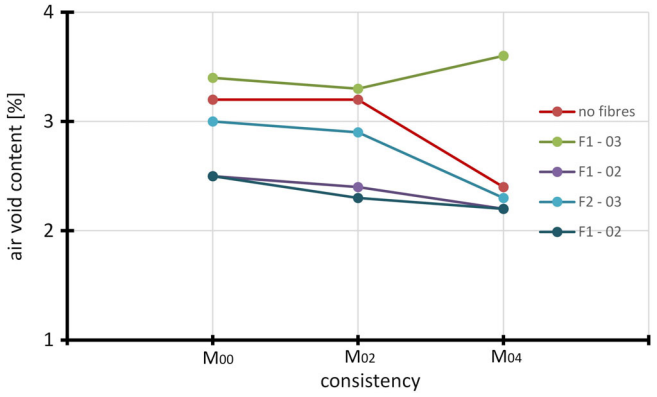

FIGURE 2 Air void content of the UHPFRC mixture of each configuration. UHPFRC, ultra high performance fiber-reinforced concrete

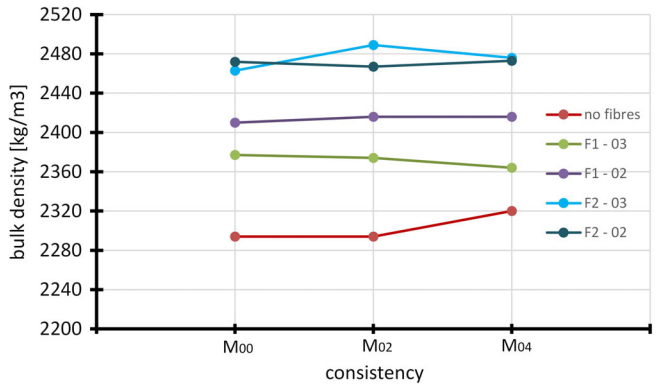

FIGURE 3 Bulk density of the fresh UHPFRC-mixture of each configuration. UHPFRC, ultra high performance fiber-reinforced concrete

Spread flow, bulk density and air void content of each configuration were measured for the fresh concrete directly after mixing. The spread flow was determined by using a Hagermann cone. As illustrated in Figure 1, the spread flow increases when increasing the PCE-amount. The spread flow of the mixtures with 03-fibers was always greater than the mixtures with 02-fibers when fixing the remaining parameters. This can be explained by the increased specific fiber surface area in the systems with thinner fibers. The surface will be covered with a water film during the mixing procedure. The water is absorbed from the pore solution resulting in a lower spread flow.

The air void content (Figure 2) and the bulk density (Figure 3) were measured by using a 1 L bowl and pressure gauge method. The minimal air void content is observed for F1. Decreasing the viscosity of the concrete reduces the air void content. The mixture F1-03 shows an exceptional behavior.

The bulk density slightly increases when reducing the viscosity of concrete without fibers. In mixtures with fibers, bulk densities are nearly independent of the viscosity (with the exception of mixture F1-03).

For every configuration, six specimens of size $40 \times 40 \times 160$ mm were produced, three cast from the side (denoted by s) and three from the middle (denoted by m) of the formwork, see Table 2 for a summary. After

TABLE 3 Bending tensile strength and compression strength of the mixtures without fiber-reinforcement

Mixture/consistency	M00	M02	M04
Bending tensile strength (MPa)	11.58	13.77	15.46
Compression strength (MPa)	157.5	150.2	150.7

TABLE 2 Overview of specimens and notation

	Fiber dimension			Consistency		
Fiber volume fraction (%)	Length l_f (mm)	Diameter d_f (mm)	Casting method	M00 100% PCE	M02 110% PCE	M04 120% PCE
1	12.5	0.2	s	M00F1s02	M02F1s02	M04F1s02
1	12.5	0.2	m	M00F1m02	M02F1m02	M04F1m02
1	12.5	0.2	s	M00F2s02	M02F2s02	M04F1s02
1	12.5	0.2	m	M00F2m02	M02F2m02	M04F1m02
2	12.5	0.3	s	M00F1s03	M02F1s03	M04F1s03
2	12.5	0.3	m	M00F1m03	M02F1m03	M04F1m03
2	12.5	0.3	s	M00F2s03	M02F2s03	M04F1s03
2	12.5	0.3	m	M00F2m03	M02F2m03	M04F1m03

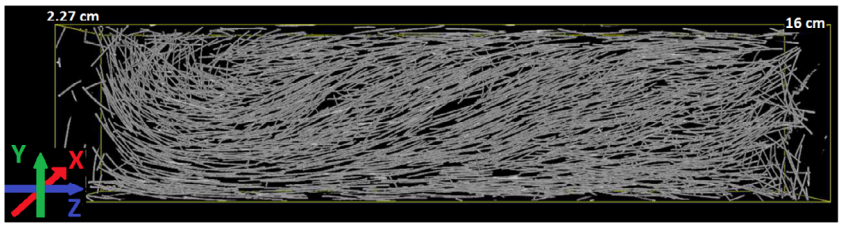

FIGURE 4 3D coordinate system and fiber system reconstruction of a subvolume of specimen M00F1s03

production, the specimens were cured in a climate chamber for 28 days.

Additionally, control specimens without fiber-reinforcement were produced and tested to determine the mechanical properties of the three mixtures. Bending tensile strength and compression strength are given in Table 3. The modulus of elasticity is about 50 GPa for all three mixtures.

2.2 | µCT imaging

One of the three specimens for each configuration was scanned by micro computed tomography (µCT) at the Fraunhofer Institut für Techno- und Wirtschaftsmathematik (ITWM) in Kaiserslautern, Germany. To reduce gray value variations in the images, the prismatic specimens were inserted into a cylindrical UHPC shell for scanning. The CT tube was a Feinfocus FXE 225.51 with a maximum acceleration voltage of 225 kV and maximum power of 20 W. A Perkin Elmer detector XRD 1621 with 2048 × 2048 pixels was used. The tube voltage was 190 kV, the target electricity 65 µA, and the power 12 W. Tomographic reconstructions were obtained from 800 projections. The voxel edge length is 90.6 µm. Consequently, the reconstructed images contain 441 × 441 × 1,766 pixels.

Figure 4 shows a visualization of one specimen together with the coordinate system that has been used for the analysis. The Y-direction describes the height of the specimen with Y = 0 at the bottom. The Z-direction describes the length of the specimen. Casting from the side is performed from Z = 0 mm and Y = 40 mm. The casting point for casting from the middle was at Z = 80 mm and Y = 40 mm.

2.3 | Bending tests

The bending behavior of all produced specimens was investigated by four point bending tests on unnotched specimens as shown in Figure 5. For testing, specimens were rotated by 90° about the Z-axis such that the concrete surface pointed to the front. The bending tests were carried out in a displacement-controlled manner. The load rate was chosen very low at 0.1 mm/min to be able

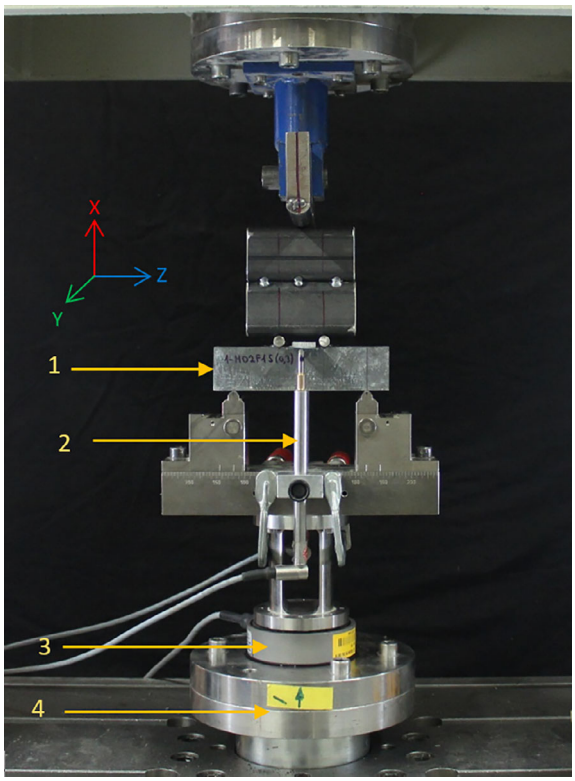

FIGURE 5 Setup of the four-point bending test (1 = the specimen, 2 = extensometer on both sides to measure the deflection in the midspan, 3 = force gauge, 4 = load cell)

to follow the crack formation. The displacement in the midspan was measured by using an extensometer. The test ended as soon as a deflection of 5 mm in the midspan was reached.

3 | IMAGE ANALYSIS

3.1 | Image processing

For image processing, the software MAVI (Modular Algorithms for Volume Images)[15] was used. In a first step, illumination gradients from the specimen edges to the center were removed. For this purpose, a mean filter[16] was applied. The filter mask was chosen as a cube with an edge length equal to the diameter of the largest pore in the

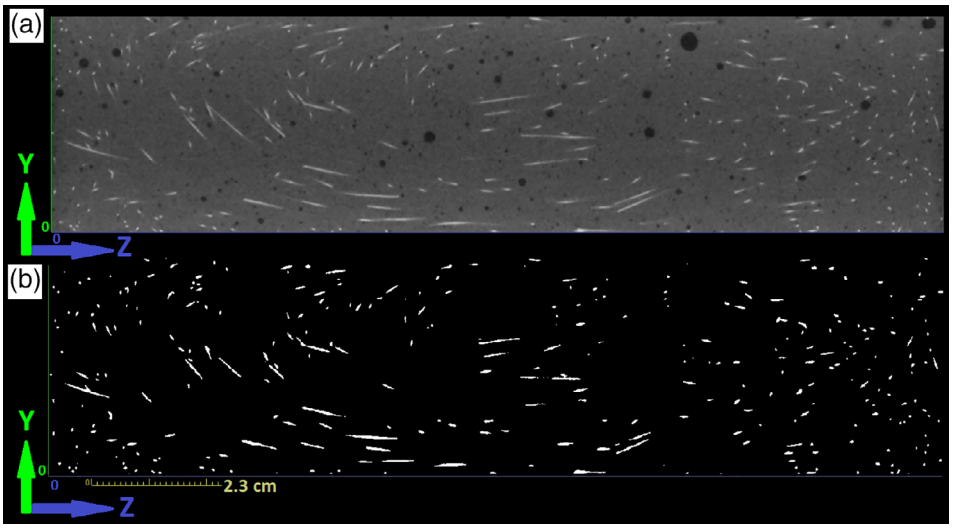

FIGURE 6 Sectional image of the CT image of specimen M00F1s03 (a). Fibers are white, concrete matrix is gray, and air pores are black. Binarisation of the fiber system (b)

image. Subtraction of the resulting image from the original image homogenized the gray value distribution such that the fiber system could be binarised. The threshold for binarisation was chosen globally by using Otsu'smethod.[17] Sectional images of one of the 3D images obtained by μCT and the binarisation result are shown in Figure 6.

3.2 | Fiber content

To assess the homogeneity of the spatial fiber distribution w.r.t the coordinate directions X, Y, or Z, we consider the area fraction profile (AFP). It represents the area fraction of the fibers in each slice orthogonal to the given coordinate direction. For macroscopically homogeneous microstructures, the expected area fraction in a 2D slice equals the volume fraction of the specimen. Significant variations of the area fraction indicate spatial inhomogeneities such as layered structures or structures with a gradient. Due to the partial volume effect[18] in the CT imaging and the low resolution of the images (2–3 pixels per fiber diameter), estimated fiber volume fractions deviate from the theoretical ones. As the difference is more pronounced for thinner fibers, we will consider centered AFPs for better comparability. That is, we subtract the empirical volume fraction of the given specimen from the computed area fractions in the slices. To improve visual comparability, the AFPs are smoothed by exponential smoothing with the parameter $\alpha = 0.05$ (R function HoltWinters, R package stats[19]), see Figure 7 for an example.

3.3 | Fiber orientation

To estimate the local orientation of the fibers, we use a method based on partial second derivatives.[20] See

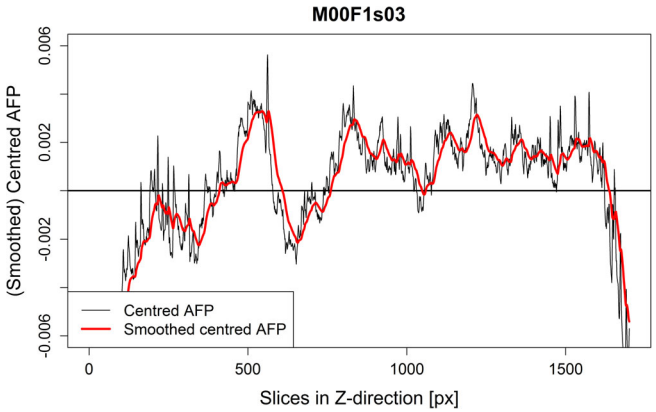

FIGURE 7 Centered area fraction profile of M00F1s03, smoothed version in red

Herrmann and Pastorelli[21] for an application to steel fiber reinforced concrete. For reducing the noise, the gray value image f was smoothed by application of an isotropic Gaussian convolution filter with kernel g_σ at scale σ. Then, the second order derivatives

$$f_{ij} = \frac{\partial^2}{\partial i \partial j}(f * g_\sigma), i,j \in \{x,y,z\}$$

of the filtered image are computed to obtain the Hessian matrix

$$H(f) = \begin{pmatrix} f_{xx} & f_{xy} & f_{xz} \\ f_{yx} & f_{yy} & f_{yz} \\ f_{zx} & f_{zy} & f_{zz} \end{pmatrix}.$$

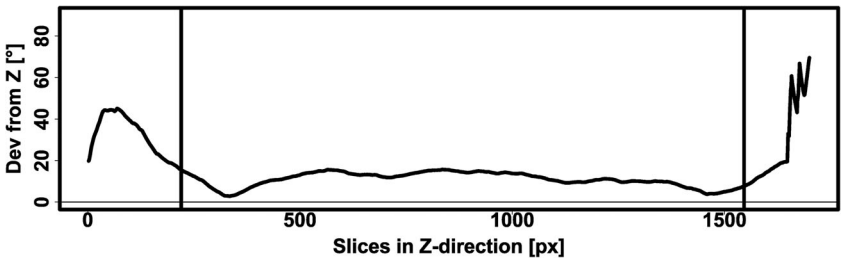

FIGURE 8 Deviation (Dev) of the fiber orientation from the Z-axis (in degree) in each slice along the Z-direction of specimen M00F1s03. Slices outside the range marked by the vertical lines are neglected in the subsequent analysis

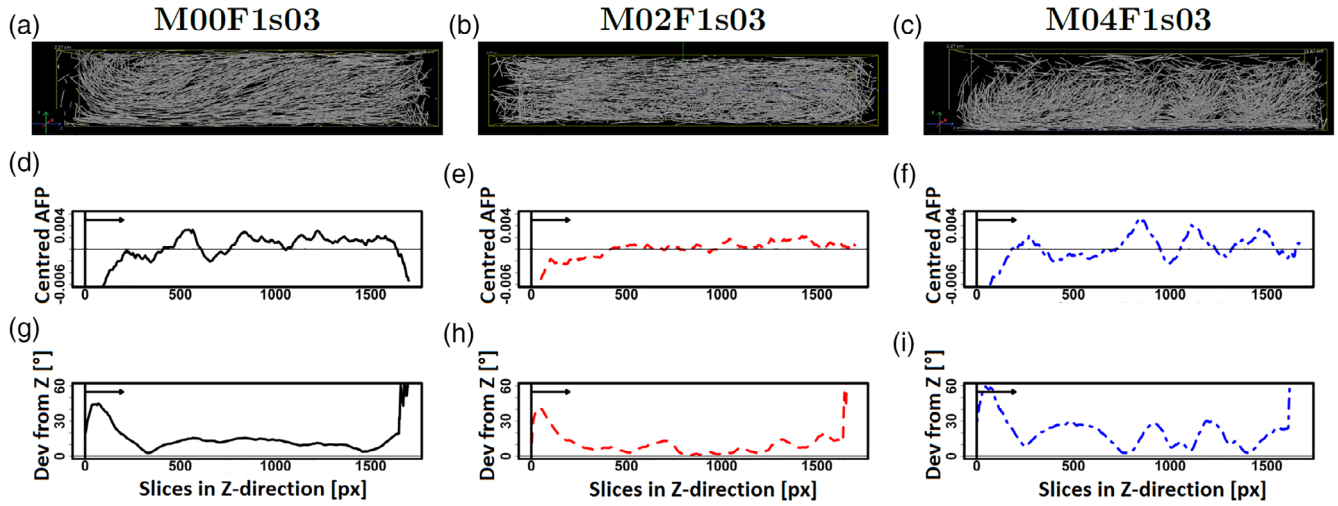

FIGURE 9 Volume rendering (a, b, c), centered AFP along the Z-direction (d, e, f), and deviation of the fiber orientations from the Z-axis along the Z-direction (g, h, i) of specimens M00F1s03, M02F1s03 and M04F1s03. The casting point is marked with a vertical line and the flow direction is illustrated by arrows. AFP, area fraction profile

σ is chosen equal to the radius of the fibers.[20] In each fiber pixel p, the eigenvector of H w.r.t. the smallest eigenvalue yields an estimate of the local fiber orientation in p. For averaging the fiber orientations (x_i, y_i, z_i) over a slice of the 3D image, the orientation matrix[22]

$$T = \begin{pmatrix} \sum_i x_i^2 & \sum_i x_i y_i & \sum_i x_i z_i \\ \sum_i x_i y_i & \sum_i y_i^2 & \sum_i y_i z_i \\ \sum_i x_i z_i & \sum_i y_i x_i & \sum_i z_i^2 \end{pmatrix}$$

is computed. The eigenvector corresponding to the largest eigenvalue of T yields the principal orientation within the slice. In our application, an alignment of the fibers along the tensile axis, here the Z-axis, is desired. Hence, we consider the slicewise deviation of the fiber orientations from the Z-axis, see Figure 8 for an example. The large deviations at the edges of the specimen can be explained by formwork effects. Hence, on each side an edge area of 2 cm width (220 slices) is neglected in the statistical analysis.

4 | RESULTS

4.1 | Image analysis

Figure 9 shows a comparison of specimens with different consistencies (controlled by the amount of PCE-plasticizer) while the other parameters (fiber content, fiber diameter and casting point) are fixed. The M02-specimen shows the most homogeneous fiber system w.r.t. the area fraction and the fiber orientation. The very fluid consistency of M04 results in fluctuations in the spatial distribution and orientation of the fibers. The volume rendering also clearly shows the sedimentation of the fibers. The more viscous M00-specimen shows some inhomogeneities close to the casting point and a more homogeneous structure in the second half of the specimen.

Figure 10 shows the centered AFPs along the Y-direction, that is, from the bottom to the top of the specimens. All specimens show sedimentation of the fibers which is most pronounced for the M04-specimens. The M00- and M02-specimens often show a similar behavior. The sedimentation is most pronounced for the thicker, hence

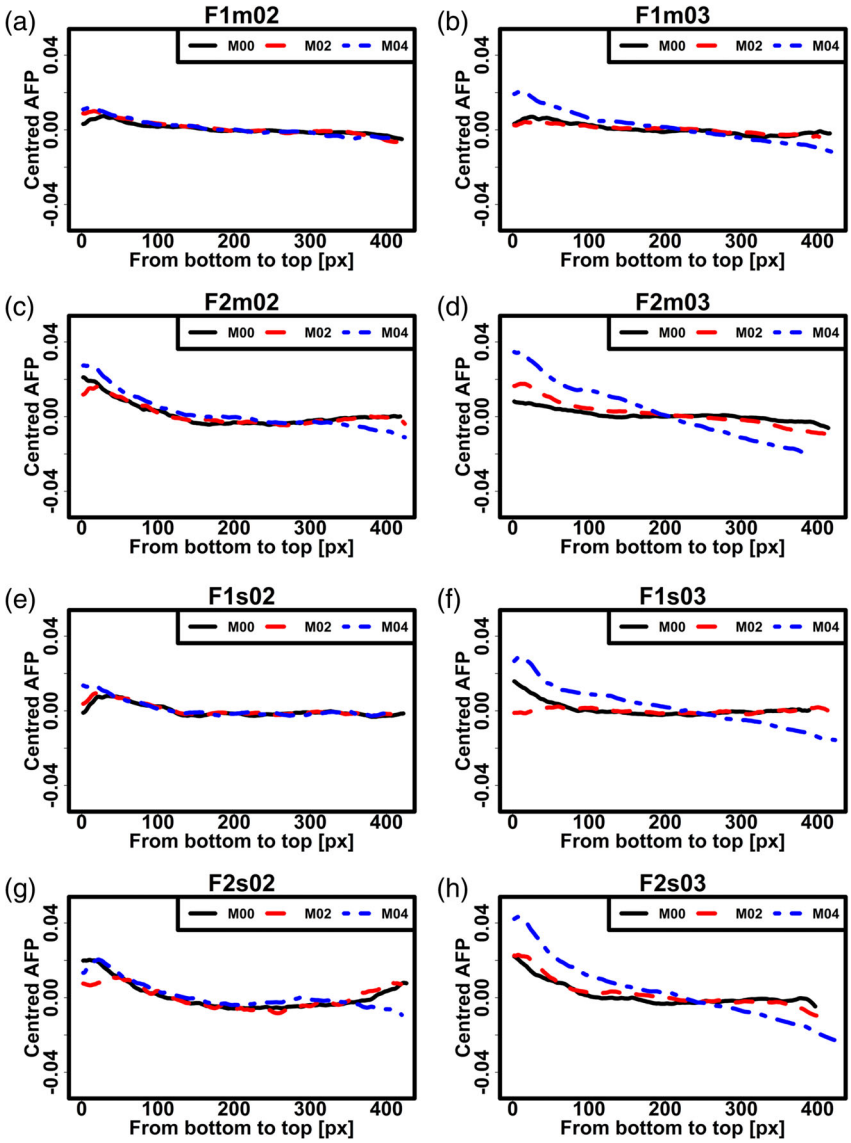

FIGURE 10 Centered AFP along the Y-direction (from bottom to top). AFP, area fraction profile

heavier, fibers ($d_f = 0.3$ mm). The casting method does not seem to have any influence.

AFPs along the X-direction, that is, from right to left, are shown in Figure 11. The specimens generally show some wall effects close to the boundary of the formwork. Specimens with high volume fraction (F2) and thin fibers ($d_f = 0.2$ mm) are most affected. Consistency and casting method do not seem to contribute to the wall effect.

Finally, AFPs along the Z-direction are shown in Figure 12. The strongest variations are observed for the M04-specimens. Casting from the middle leads to an almost symmetric AFP with an accumulation of fibers in the center of the specimens. M02-specimens cast from the side show less fluctuations except for F2s02-specimens.

For studying the alignment of the fibers we plot the local deviations of the fiber orientation from the Z-axis in Figure 13. The maximal deviation was approximately 45°. Casting from the side results in a more homogeneous fiber orientation distribution than casting from the middle. In the latter case, the deviation of the fibers from the Z-axis is low just in a narrow region around the casting point and increases in the flow directions toward the sides. This deviation seems to be stronger for viscous mixtures with few, thin fibers. For more and/or thicker fibers this effect is reduced. The fiber orientation of s03-specimens is highly affected by the consistency (independent of the volume fraction). Fluid mixtures lead to more fluctuations. For 02-specimens, the correlation between fiber orientation and consistency is not pronounced. The orientation of fibers in s02-specimens deviates least from the Z-axis for all consistencies and fiber volume fractions.

To measure the variation in the spatial distribution and orientation of the fibers in a specimen, the sample standard deviation (SSD) of the centered AFPs and the orientation deviations in Z-direction (Figures 12 and 13)

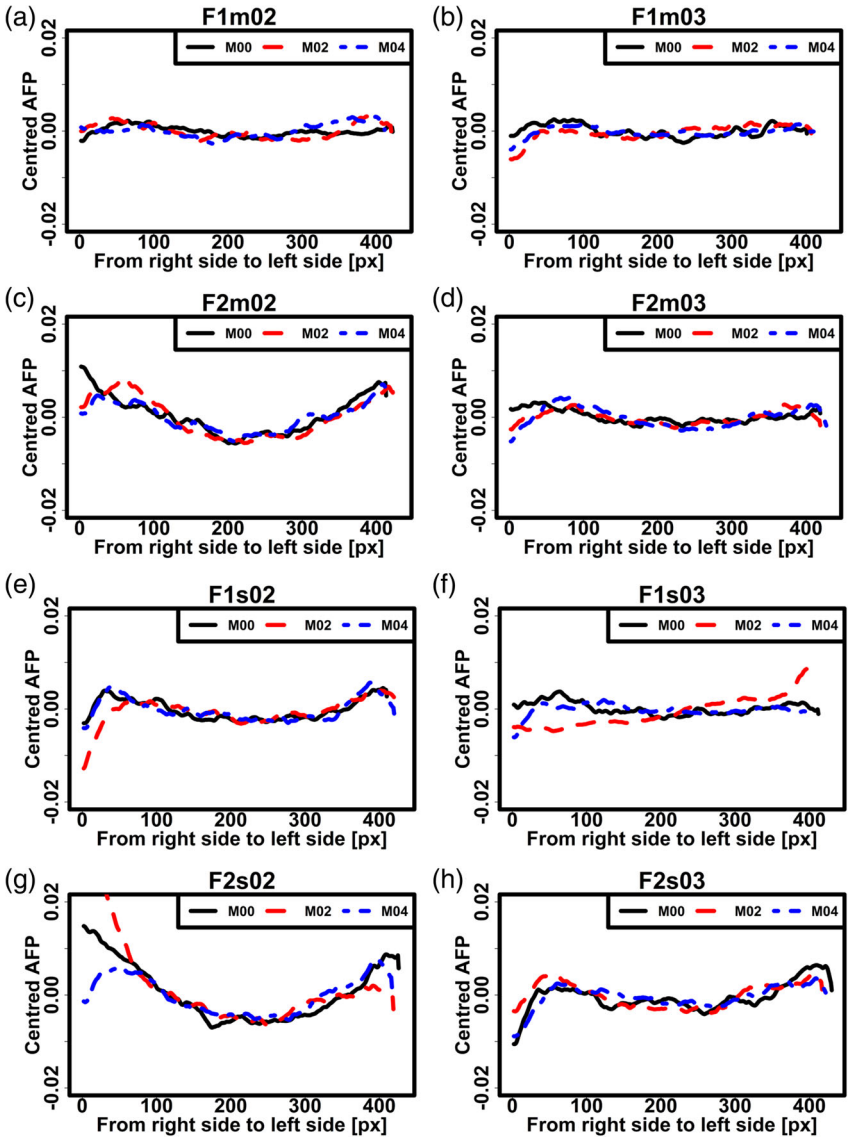

FIGURE 11 Centered AFP along the X-direction (from right side to left side). AFP, area fraction profile

were calculated. The results are visualized in Figure 14. Again, M04-specimens are found to be most heterogeneous. The SSDs are maximized in this group. Additionally, they show the highest differences between the four sets of fiber parameters used. In total, fiber systems are more homogeneous when casting from the side than when casting from the middle. With respect to the fiber orientation, the s-specimens are clearly more aligned to the Z-axis than the m-specimens. Figure 15 showing the SSDs along the Y-direction confirms the visual impression that the spatial fiber distribution and fiber orientation of M04-specimens are inhomogeneous compared to M00- and M02-specimens for all fiber volume fractions, fiber diameters, and casting methods considered.

In summary, M00- and M02-specimens cast from the side are most homogeneous w.r.t. fiber orientation and spatial distribution.

4.2 | Bending tests

During the testing of the 72 specimens (three specimens for each of the 24 parameter combinations), load-midspan deflection curves were recorded (see Figures 16 and 17). All specimens showed deflection-hardening performance to different extent.

In the initial phase, the bending behavior of the specimens is linear elastic. When the load exceeds the matrix tensile strength, a first crack occurs in the weakest point of the matrix in the middle third of the specimen. After crack initiation, the fibers bridging the crack get activated and avoid propagation of the crack opening. The response curve remains in the linear elastic range and the tensile stress increases at the bottom of the specimen. In the same manner, the specimen may develop three to four visible cracks. Crack propagation occurs at different

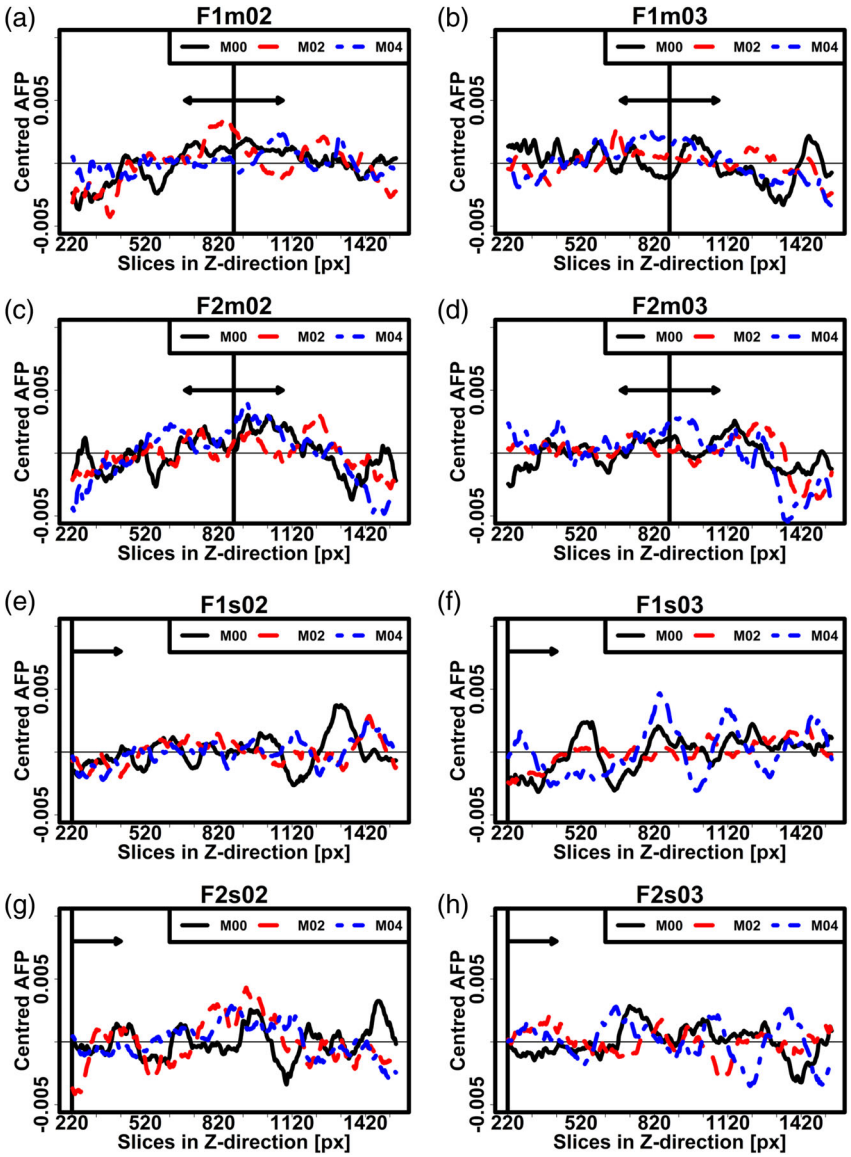

FIGURE 12 Centered AFP along to the Z-direction without edge area. The casting point is marked with a vertical line and the flow direction is illustrated by arrows. AFP, area fraction profile

scales. The response behavior of the specimen is still elastic or elastoplastic but linear. This will be followed by non-linear behavior, where many cracks propagate simultaneously until reaching the maximum load. A mean strain constitutive law can be assumed, because the complete cross sections are strained along the specimen, which concurs with the AFGC-Recommendation.[23]

When reaching the maximum load, the crack which requires a minimum energy to develop break down dominates the process. That is, crack propagation progresses only in the dominating crack and the response behavior is non-linear and plastic. Simultaneously, other cracks reduce in width causing a stress relief on both sides of the dominating crack. Thus, a rigid body motion of the two parts of the specimen is the dominant mechanism such that a crack width law can be assumed. This is in line with Prudencio et al.[24] and the AFGC-Recommendation.[23] The residual width of the other cracks depends on the deformation degree reached before, which could be elastic or elastoplastic. Figure 16 shows the load-midspan deflection curves for different consistencies of F1-specimens. Maximal force values are observed for the M02-specimen which has the most homogeneous fiber system. In contrast, the M04-specimen with strong sedimentation of fibers is least stable. Similar results have been obtained for F2-specimens cast from the middle.

The load-deflection curves for all specimens are shown in Figure 17. Typically, the first crack occurs at a deflection between 0.06 and 0.08 mm and the maximum linear stress is reached at a deflection between 0.17 and 0.22 mm. In all cases, specimens with higher fiber volume fraction (F2, dark colors) turn out to be more stable than those with only 1% volume fraction (F1, bright colors). For fixed volume fraction, specimens with thin (hence, more) fibers yielded better

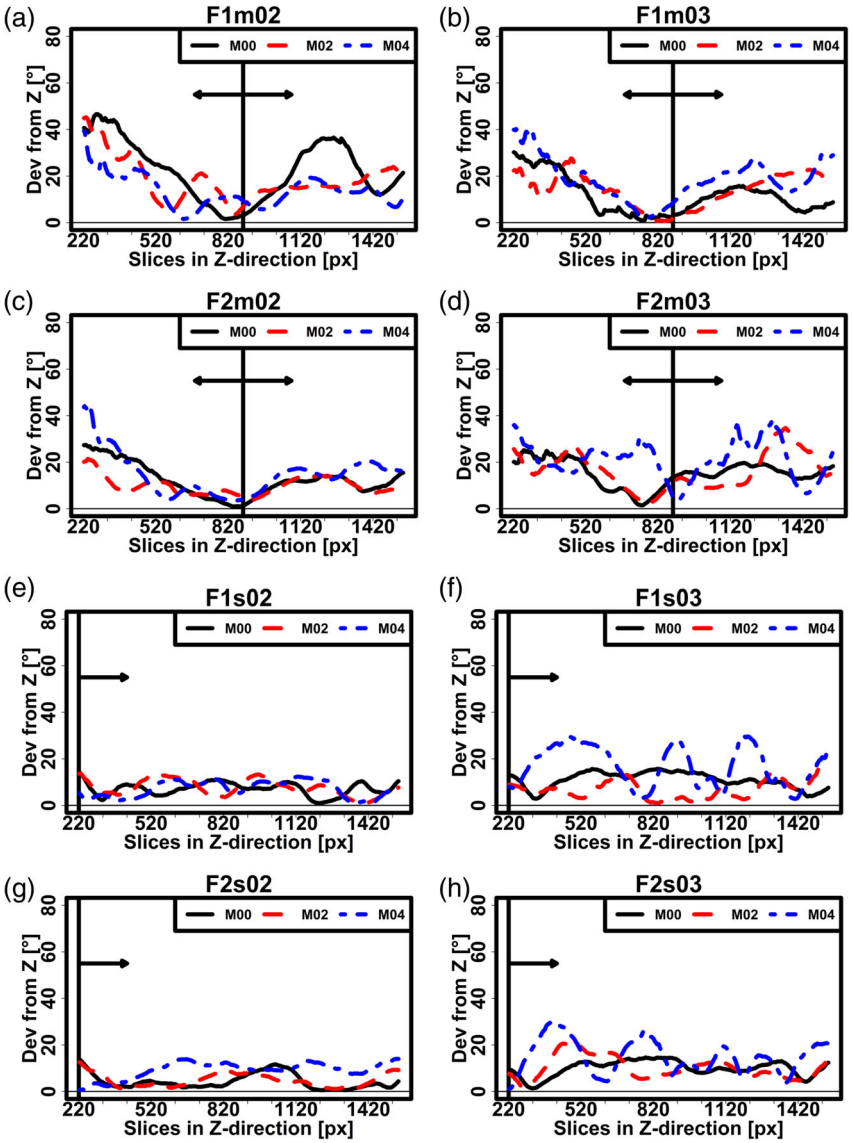

FIGURE 13 Deviation of the fiber orientations from the Z-axis along the Z-direction (without edge area). The casting point is marked with a vertical line and the flow direction is illustrated by arrows

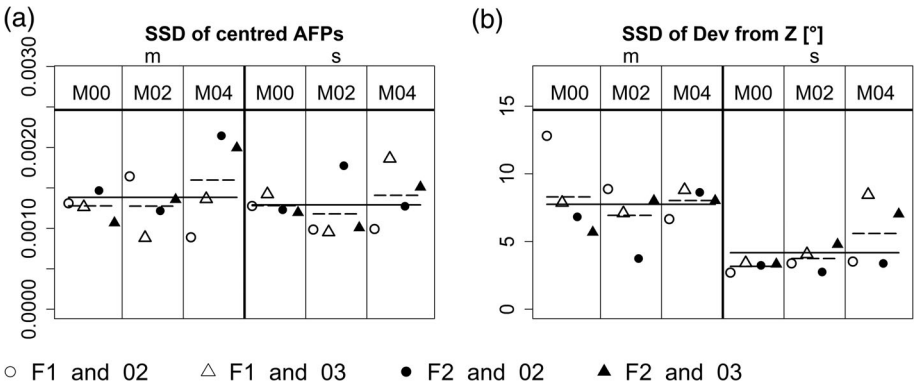

FIGURE 14 SSD of the centered AFP (a) and the deviation of the fiber orientation from the Z-axis (b) along the Z-direction. The mean value over all specimens with the same casting method is given as solid horizontal line. Dashed lines describe mean values in subgroups with fixed casting point and plasticizer content but varying fiber parameters. AFP, area fraction profile; SSD, sample standard deviation

bending performance than specimens with thick fibers. M04-specimens clearly show a reduced mechanical stability while M00- and M02-specimens are comparable. The variation between the curves for the three specimens with the same parameters is small compared to the overall variability.

For further comparison of the specimens, the elastic flexural load F_{el} is considered. It corresponds to the force

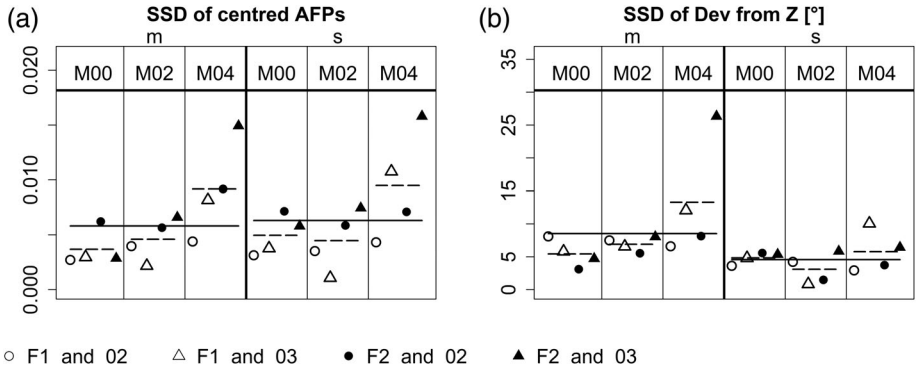

FIGURE 15 SSD of the centered AFP (a) and the deviation of the fiber orientation from the Z-axis (b) along the Y-direction. Dashed lines describe mean values in subgroups with fixed casting point and plasticizer content but varying fiber parameters. AFP, area fraction profile; SSD, sample standard deviation

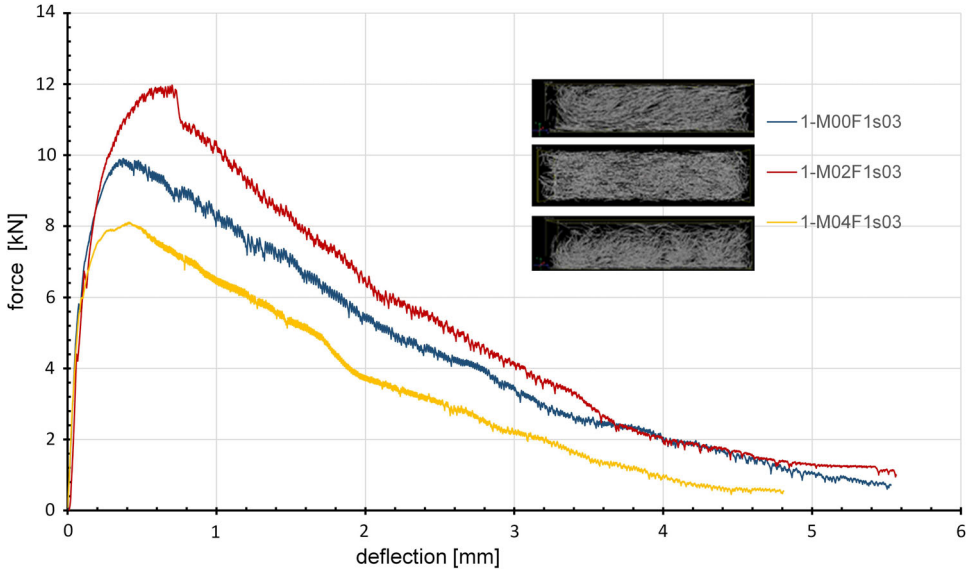

FIGURE 16 Load-midspan deflection curves for the specimens M00F1s03, M02F1s03 and M04F1s03

value at which the curve enters a non-linear phase. From F_{el}, the elastic flexural strength f_{el} can be computed by

$$f_{\mathrm{el}} = \frac{3F_{\mathrm{el}}}{a^2} \tag{1}$$

where $a = 4$ cm is the specimens' cross section edge length. The elastic flexural strengths for the tested specimens are summarized in Figure 18.

In general, the m-specimens show reduced elastic strengths compared to s-specimens. The difference between m- and s-specimens reduces when increasing the fiber volume fraction. For fixed fiber volume fraction, the specimens with reduced fiber diameter, hence, containing more fibers, show a better performance. Irrespectively of the casting method and the fiber parameters, the maximal elastic flexural strength is obtained for the M02-specimens. The difference between M00-specimens and M02-specimens is typically small. M04-specimens show the lowest strength which can be explained by the inhomogeneities in the fiber system due to sedimentation.

4.3 | Discussion

The casting process causes a turbulence in the vicinity of the casting point, which produces a heterogeneous fiber geometry in this region. The flux seems to get laminar a few centimeters (around 2–6 cm) after the casting point. The spatial fiber distribution becomes homogeneous and the fibers align in flow direction. The degree of alignment depends mainly on the consistency of the mixture.

Fibers in M00-specimens keep their orientation caused by turbulent flux in the vicinity of the casting point because the viscosity of the matrix is high enough to prevent the realignment of the fibers by their own weight. This realignment is possible with consistency M02 resulting in homogeneous fiber systems even close to the casting point. In contrast, the very low viscosity of the M04-mixture leads to fluctuations and sedimentation. The flexural strength observed during the bending test correlates well with the observed homogeneity of the specimens. M02-specimens achieved the highest strength followed by M00-specimens.

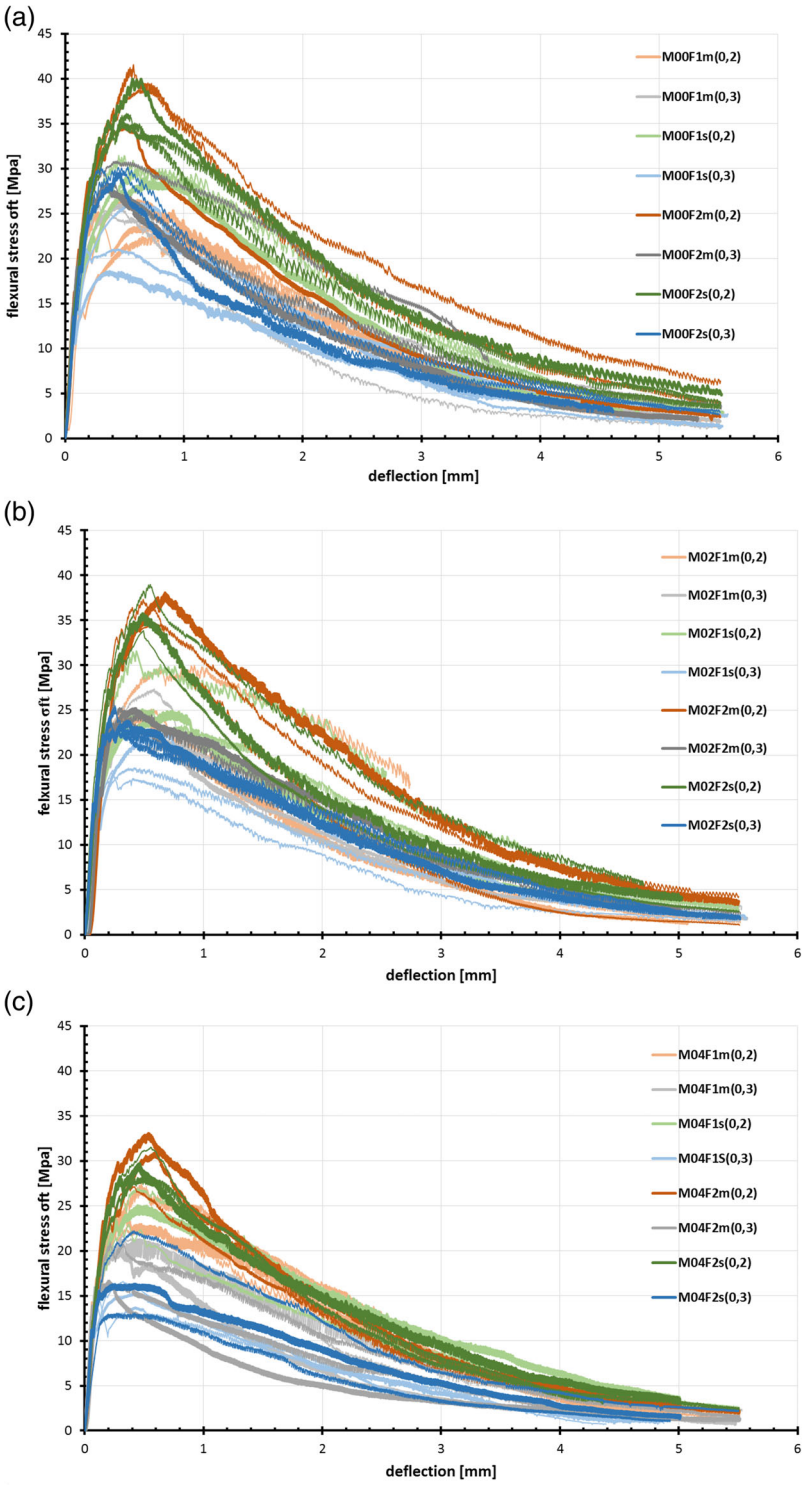

FIGURE 17 Flexural stress–deflection curves of all tested specimens grouped by consistencies M00 (a), M02 (b) and M04 (c)

5 | CONCLUSION

The study presented in this paper investigates the influence of production parameters on the fiber geometry and, as a consequence, on the flexural behavior of UHPFRC. The fiber geometry in specimens with different production parameters was investigated by means of micro computed tomography. Subsequently, the flexural behavior of the specimens was investigated in four point bending tests. The following conclusions could be drawn:

- Casting from the side results in a more homogeneous fiber geometry than casting from the middle. This results in a better mechanical performance.
- Increasing the fiber radius from $d_f = 0.2$ mm to $d_f = 0.3$ mm increases the inhomogeneity in the fiber

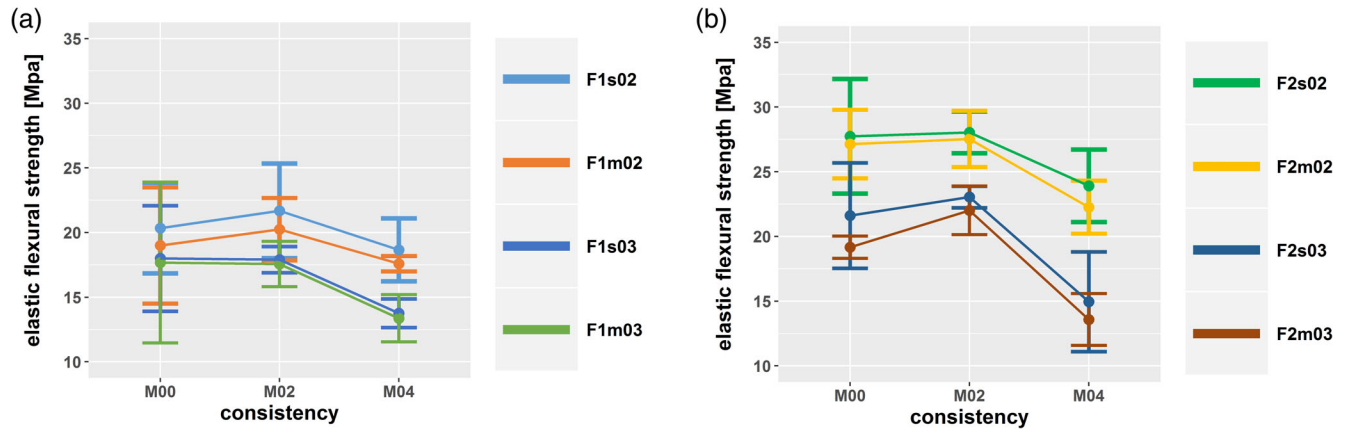

FIGURE 18 Correlation between the studied parameters and elastic flexural strength. Dots are the means of the elastic flexural strengths of the three specimens with equal parameters. The error bars represent the 95% confidence interval of the mean

systems. In particular, sedimentation is more pronounced for thicker fibers.

- Fiber orientation stabilizes after a certain distance from the casting point. This is consistent with findings by Vandewalle et al.[13] and Ferrara et al.[14] In our experiments, a unidirectional alignment of the fibers with deviations of a few degrees from the flow direction can be assumed approx. 2–6 cm after the casting point for not too fluid consistencies (M00 or M02).
- The most homogeneous fiber systems resulting in the highest flexural strength were obtained using the M02 mixture with a spread flow (Hagermann cone) between 27 and 28 cm. Mixtures with lower spread flow (25–27 cm) can deliver good results, too. If the spread flow exceeds 28 cm, significant sedimentation of the fibers is observed which decreases the flexural strength. These findings are in line with the results by Wang et al.[11] and Stähli et al.[12]
- A wall effect could be observed close to the boundary of the formwork (5–10 mm). Wall effects are stronger for increasing volume fraction and decreasing fiber diameter. Casting from the middle results in reduced wall effects compared to casting from the side. This is probably correlated with the lower flow distance of the material.

The work by Herrmann and Lees[25] indicates that the surface properties of the formwork also need to be taken into account when designing the casting technology for UHPFRC specimens. Due to the observed wall effects, it remains an open question to which extent our findings can be generalized to larger samples, see Herrmann et al.[26] for a discussion. To investigate this question in the framework presented here, larger samples have been produced and will be analyzed in a subsequent study. Due to the limited sample size that can be handled by μCT, specimens have to be cut into smaller cuboids before scanning which increases the experimental effort for such investigations. To allow for an investigation of large concrete elements (e.g., beams), models and methods from spatial statistics could be used to predict the concrete geometry at a given position from a limited number of samples.

Numerical flow simulation provides an alternative approach for predicting the fiber geometry of UHPFRC samples for given production parameters.[27,28] Simulation based approaches can reduce the effort of such investigations compared to the production, characterization and testing of large amounts of concrete samples. However, the simulations should be validated by experiments. The image analysis tools presented in this work yield statistical information that can be compared to fiber parameters observed in simulations. Additionally, the statistical information can be used to fit a stochastic geometry model to the observed microstructures, for example, a system of cylinders of random orientation and position, see Redenbach and Vecchio.[29] Such models allow for the generation of virtual concrete samples with a large range of geometric characteristics. From these, mechanical properties of the concrete can be predicted by using suitable concrete models.

ACKNOWLEDGMENTS

We acknowledge support by the Deutsche Forschungsgemeinschaft (DFG) within the RTG 1932 “Stochastic Models for Innovations in the Engineering Sciences.”

ORCID

Kasem Maryamh https://orcid.org/0000-0001-5630-8889

Konstantin Hauch https://orcid.org/0000-0002-2333-5191
Claudia Redenbach https://orcid.org/0000-0002-8030-069X

REFERENCES

1. Fehling E, Schmidt M, Teichmann T, Bunje K, Bornemann R, Middendorf B. Entwicklung, Dauerhaftigkeit und Berechnung Ultrahochfester Betone (UHPC). Schriftenreihe Baustoffe und Massivbau, Heft Nr. 1. Kassel: Kassel University Press GmbH, 2005.
2. Hoàng KH, Hadl P. A new mix design method for UHPC based on stepwise optimization of particle packing density; 2016.
3. Stürwald S. Rissentwicklung bei kombiniert bewehrten UHPC-Balken. 53. Forschungskolloquim DAfStb. Kassel: Kassel University Press GmbH, 2008.
4. Leutbecher T. Rissbildung und Zugtragverhalten von mit Stabstahl und Fasern bewehrtem Ultrahochfesten Beton (UHPC). Kassel: Kassel University Press GmbH, 2008.
5. DAfStb-Heft 561. *Sachstandsbericht Ultrahochfester Beton*. Beuth, 2008.
6. Fröhlich S, Schmidt M. Rheologische Eigenschaften von Faserhaltigem Ultrahochfestem Beton. 53. Forschungskolloquim DAfStb. Kassel: Kassel University Press GmbH, 2008.
7. Wille K, Parra-Montesinos GJ. Effect of beam size, casting method, and support condition on flexural behavior of ultra-high-performance fibre-reinforced concrete. ACI Mater J. 2012; 109(3):379–388.
8. Schnell J, Schladitz K, Frank S. Richtungsanalyse von Fasern in Betonen auf Basis der Computer-Tomographie. Beton- und Stahlbetonbau. 2010;105:72–77.
9. Lange J, Rauscher S, Benning W, Hegger J. Ellipsen- und Kreisdetektion zur Bestimmung der Orientierung von Stahl- und Glasfasern in Beton. TM-Tech Mess. 2008;75:529–536.
10. Scheffler B, Schmidt M. Application of ultra-high performance concrete for multifunctional road pavements. Proceedings of Hipermat 2012 - 3rd International Symposium on UHPC and Nanotechnology for High Performance Construction Materials. Kassel: Kassel University Press GmbH; 2012.
11. Wang R, Gao X, Huang H, Han G. Influence of rheological properties of cement mortar on steel fiber distribution in uhpc. Construct Build Mater. 2017;144:65–73.
12. Stähli P, Custer R, van Mier JGM. On flow properties, fibre distribution, fibre orientation and flexural behaviour of FRC. Mater Struct. 2008;41:189–196. https://doi.org/10.1617/s11527-007-9229-x.
13. Vandewalle L, Heirman G, Van Rickstal F. Fibre orientation in self-compacting fibre reinforced concrete. Proceedings of the 7th International RILEM Symposium on Fibre Reinforced Concrete: Design and Applications; R. Gettu (ed), India. Chennai: RILEM Publications; 2008, p. 719–728.
14. Ferrara L, Ozyurt N, di Prisco M. High mechanical performance of fibre reinforced cementitious composites: The role of "casting-flow induced" fibre orientation. Mater Struct. 2011;44: 109–128.
15. Department of Image Processing Fraunhofer Institute for Industrial Mathematics ITWM. MAVI - Modular algorithms for volume images. Kaiserslautern, Germany; 2005. www.mavi-3d.de.
16. Soille P. Morphological image analysis. Berlin, Heidelberg: Springer-Verlag; 2004.
17. Otsu N. A threshold selection method from gray-level histograms. IEEE Trans Syst Man Cybern. 1979;9(1):62–66.
18. Heckel F, Meine H, Moltz JH, et al. Segmentation-based partial volume correction for volume estimation of solid lesions in CT. IEEE Trans Med Imaging. 2014;33(2):462–480.
19. R Core Team. *stats: R statistical functions*. R Foundation for Statistical Computing, Vienna, Austria, 2019.
20. Wirjadi O, Schladitz K, Easwaran P, Ohser J. Estimating fibre direction distributions of reinforced composites from tomographic images. Image Anal Stereol. 2016;35(3):167–179.
21. Pastorelli E, Herrmann H. Time-efficient automated analysis for fibre orientations in steel fibre reinforced concrete. Proc Est Acad Sci. 2016;28–36(01):65.
22. Fisher NI, Embleton BJJ, Lewis T. Statistical analysis of spherical data. Cambridge: Cambridge University Press, 1987.
23. AFGC Recommendation. Recommendations; association francais de genie civil (afgc). Documents scientifiques et technique; Ultra High Performance Firbre-Reinforced Concrete; 2013.
24. Prudencio L, Austin S, Jones P, Armelin H, Robins P. Prediction of steel fibre reinforced concrete under flexure from an inferred fibre pull-out response. Mater Struct. 2006;39:601–610.
25. Herrmann H, Lees A. On the influence of the rheological boundary conditions on the fibre orientations in the production of steel fibre reinforced concrete elements. Proc Est Acad Sci. 2016;408–413(11):65.
26. Herrmann H, Goidyk O, Naar H, Tuisk T, Braunbrück A. The influence of fiber orientation in self-compacting concrete on 4-point bending strength. Proc Est Acad Sci. 2019;337–346(08):68.
27. Gudžulić V, Dang TS, Meschke G. Computational modeling of fiber flow during casting of fresh concrete. Comput Mech. 2019;63:1111–1129.
28. Kang S, Kim J. Numerical simulation of the variation of fiber orientation distribution during flow molding of ultra high performance cementitious composites (uhpcc). Cem Concr Compos. 2012;34(2):208–217.
29. Redenbach C, Vecchio I. Statistical analysis and stochastic modelling of fibre composites. Compos Sci Technol. 2011;71(2): 107–112.

AUTHOR BIOGRAPHIES

Kasem Maryamh, MSc, Faculty of Civil Engineering, Technische Universität Kaiserslautern, Institute of Concrete Structures and Structural Design, Paul-Ehrlich-Straße 14, D-67663 Kaiserslautern, Germany. Email: kasem.maryamh@bauing.uni-kl.de

Konstantin Hauch, MSc, Faculty of Mathematics, Technische Universität Kaiserslautern, Department of Mathematics, Gottlieb-Daimler-Straße 47, D-67663 Kaiserslautern, Germany. Email: hauch@mathematik.uni-kl.de

Prof Dr Claudia Redenbach, Faculty of Mathematics, Technische Universität Kaiserslautern, Department of Mathematics, Gottlieb-Daimler-Straße 47, D-67663 Kaiserslautern, Germany. Email: redenbach@mathematik.uni-kl.de

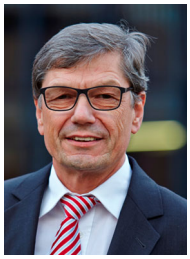

Prof Dr -Ing Jürgen Schnell, Faculty of Civil Engineering, Technische Universität Kaiserslautern, Institute of Concrete Structures and Structural Design, Paul-Ehrlich-Straße 14, D-67663 Kaiserslautern, Germany. Email: juergen.schnell@bauing.uni-kl.de

How to cite this article: Maryamh K, Hauch K, Redenbach C, Schnell J. Influence of production parameters on the fiber geometry and the mechanical behavior of ultra high performance fiber-reinforced concrete. *Structural Concrete*. 2020; 1–15. https://doi.org/10.1002/suco.202000105